Energy & Environmental Science

ROYAL SOCIETY OF CHEMISTRY

PAPER

View Article Online
View Journal | View Issue

Cite this: *Energy Environ. Sci.*, 2026, **19**, 2910

3D imaging-informed electrode engineering for water splitting

Shuhao Wang,[a] Omid Tavakkoli,[c] Mohamed Regaieg,[d] Christoph Sachs,[e] David Aymé-Perrot,[e] Hubert Girault,[f] Quentin Meyer,*[a] Ying Da Wang,*[b] Ryan T. Armstrong,[c] Chuan Zhao*[a] and Peyman Mostaghimi*[c]

Received 15th January 2026,
Accepted 11th March 2026

DOI: 10.1039/d6ee00290k

rsc.li/ees

Gas bubble accumulation limits mass transport in porous electrodes during alkaline water electrolysis at high current densities. Herein, synchrotron-based *operando* micro-CT and microstructure-resolved lattice Boltzmann method simulations are employed to unveil how porosity and geometric structure govern hydrogen bubble detachment and two-phase transport in alkaline water electrolysis. It is found that porous electrodes with a rationally designed ordered pore architecture enable efficient mass transport by minimizing gas trapping and promoting continuous electrolyte renewal. By contrast, commercial nickel foams with low porosity, despite their larger surface area, exhibit severe gas accumulation and poor electrode utilization. Guided by these insights, we 3D-printed a highly ordered square-grid electrode and, following catalyst deposition, achieved high-efficiency overall water splitting at 2 A cm^{-2} with a cell voltage of 2.13 V. This methodology, integrating *operando* micro-CT and lattice Boltzmann method simulations, delivers much-needed design rules for gas evolving porous electrodes and demonstrates that tuning a 3D pore architecture is critical for advanced alkaline water electrolysis.

Broader context

Green hydrogen production through water electrolysis is essential for decarbonizing hard-to-abate sectors such as steel, chemicals, and heavy transport. However, industrial-scale alkaline electrolyzers face a critical bottleneck: gas bubbles generated during operation accumulate within the porous electrodes, blocking active sites and severely limiting mass transport at high current densities required for economic viability. Understanding how an electrode architecture governs bubble behaviour has been hindered by the inability to visualize these dynamics in three dimensions during operation. Here, we combine synchrotron-based operando micro-computed tomography with advanced lattice Boltzmann simulations to directly observe hydrogen bubble evolution within porous electrodes, revealing that bubble trapping, not the surface area, is the primary performance limiter. Guided by these insights, we designed a 3D-printed electrode with an ordered pore architecture that achieves 2 A cm^{-2} at 2.13 V and ambient temperature, providing a viable pathway toward ampere-level alkaline electrolyzers. This methodology provides design rules for next-generation gas evolving electrodes and demonstrates that structural engineering is as performance-determining as catalyst selection for efficient water splitting.

1. Introduction

Gas evolving reactions are essential in modern electrochemical energy systems, such as alkaline water electrolyzers.[1,2] In particular, performances under industrial-level current densities are severely hampered due to mass transport limitations.[3,4] Under such conditions, the accumulation of gas bubbles on the electrode surface can severely hinder mass transport and compromise overall system efficiency.[5] The rate of bubble release influences not only interfacial mass transfer of reactants, namely water at the cathode and hydroxide anions at the anode, but also the uniformity of gas product transportation *via* convection.[6] To overcome these limitations, porous electrodes have been widely employed in industry.[7] The hierarchical architectures of porous media can facilitate effective gas and ion transport, reduce ohmic resistance caused by gas bubble blocking, and improve cell performance and efficiency.[8] Moreover, the interconnected pores within the porous medium can facilitate efficient bubble detachment, enabling timely gas

[a] *School of Chemistry, The University of New South Wales, Sydney, Australia. E-mail: q.meyer@unsw.edu.au, chuan.zhao@unsw.edu.au*
[b] *School of Minerals and Energy Resources Engineering, The University of New South Wales, Sydney, Australia. E-mail: yingda.wang@unsw.edu.au*
[c] *School of Civil and Environmental Engineering, The University of New South Wales, Sydney, Australia. E-mail: peyman@unsw.edu.au*
[d] *TotalEnergies, OneTech, Pau, France*
[e] *TotalEnergies SE, OneTech, Tour Coupole - 2 place Jean Millier, 92078 Paris La Défense cedex, France*
[f] *Institute of Chemical Sciences and Engineering, École Polytechnique Fédérale de Lausanne, Lausanne, Switzerland*

release during alkaline water electrolysis and stable operation under prolonged, high-rate conditions.

To ensure smooth operation at high electrolysis rates, the electrode's ability to manage convective and capillary-driven mass transport needs to be considerably improved.[9,10] In particular, the electrode structure, including specific surface area, pore density, and thickness, has a pronounced influence on gas bubble evolution reaction efficiency, such as that of the hydrogen evolution reaction (HER).[11] Nickel foams, of highly tunable porosity, are widely used as electrodes in alkaline water electrolyzers due to their high electrical conductivity, mechanical stability, and large electrochemical surface area.[12] Nevertheless, the irregular and tortuous pore network of commercial nickel foams traps gas bubbles and disrupts electrolyte flow, thereby reducing the effective active area and deteriorating reaction efficiency. Electrode structure engineering has emerged as a promising alternative to significantly improve the flow of gas and liquid within the electrode, thereby enhancing the intrinsic bubble removal efficiency of electrolyzers.[13]

Therefore, comprehensive characterization of electrode microstructure, porosity, and gas–liquid dynamics in their real environment is necessary to guide the design of next-generation high-performance alkaline water electrolyzers. In this regard, X-ray micro-computed tomography (micro-CT) is particularly promising and has notably been used to capture water formation in hydrogen fuel cells.[14,15] Compared with scanning electron microscopy (SEM), which provides sub-nanometer resolution but is confined to small fields of view, micro-CT enables multiscale structural analysis across representative electrode volumes.[16,17] While other visualization techniques, such as optical microscopy and neutron radiography, have also been employed to monitor bubble behavior, these approaches are inherently two-dimensional and cannot resolve the three-dimensional evolution of gas bubbles within porous electrodes.[18,19] Also, the low spatial resolution of lab-based micro-CT (typically 1–10 μm) and its limited temporal resolution (on the order of minutes) make it challenging to capture the rapid gas bubble nucleation, growth, and transport within microscale porous networks in alkaline water electrolyzers.[20] Therefore, the development of design guidelines for the development of next-generation alkaline water electrolyzers is currently challenged by the difficulty of capturing gas bubble dynamics in three dimensions.

Herein, we propose a synchrotron-based *operando* micro-CT imaging approach combined with the lattice Boltzmann method (LBM) to guide the structural design of porous electrodes for water electrolysis. We propose a highly ordered square-grid architecture, characterized by even pore size distribution and minimal hydrogen retention, to significantly enhance mass transport during operation. After the anode is coated with NiFe-layered double hydroxide and the cathode with Pt catalysts, the highly ordered square electrode enabled ultra-efficient overall water splitting in an alkaline electrolyzer, delivering a current density of 2 A cm^{-2} at a cell voltage of 2.13 V and ambient temperature. These findings underscore the value of LBM and *operando* micro-CT imaging-guided methodology towards the rational design of gas repelling electrodes and propose structural benchmarks for the development of next-generation porous electrodes for alkaline water electrolyzers.

2. Results

Commercial nickel foams span a broad range of pore densities (typically 5 to 130 ppi, pores per inch), which aligns with the standard structural choices employed in electrolysis and electrocatalysis research.[12] These foams feature an open-cell architecture composed of irregular metallic ligaments forming a random three-dimensional network. Here, we compare the microstructure and performance of five commercial foams with different ppi values using optical microscopy, SEM, and micro-CT (Fig. S1 to S4, SI). The pore density, described in this work as the amount of ppi (pore per inch, *i.e.,* the number of pores in a linear inch of a material), greatly varies across samples (20–130 ppi), while the beam thickness is consistently 100 μm. As a result, the porosity of the different foams, determined by micro-CT analysis, reduces from 55% to 27% as the number of ppi increases from 20 to 130 (Fig. S3, SI).

LBM simulations are then conducted to predict the liquid and gas transport pathways through these foams. Segmented micro-CT images of the nickel foams are used as the computational domain of the LBM to capture the influence of the heterogeneity of the microstructure and achieve more accurate predictions.[21] The two-phase flow simulations are conducted by first saturating the porous domain with gas, then removing it by injecting liquid and observing bubble retention. This approach captures the tendency of gas bubbles to remain trapped within nickel foams (Fig. 1a–c).

The residual hydrogen saturation is highest for the 130 ppi foam, followed by the 20 ppi foam (Fig. 1e). The 130 ppi foam possesses the smallest average pore size, which restricts gas transport and promotes gas entrapment. Meanwhile, the 20 ppi foam exhibits the largest pore size distribution, expressed here as the ratio of the smallest and largest pores, resulting in irregular pore connectivity and localized gas retention (Fig. 1f). Among the nickel foams, the 60 ppi foam provides the most balanced combination of pore size and distribution, yielding the lowest residual gas saturation. The properties of a homogeneous and well-ordered pore structure (Fig. S5, SI) were further assessed using LBM simulations, as such architectures may offer significant advantages in gas transport performance (Fig. 1d). The highly ordered square electrode demonstrates the overall lowest residual hydrogen saturation compared to commercial nickel foams, confirming its superior gas transport capability and minimal gas trapping tendency. Despite having similar pore metrics to the 60 ppi foam, the square architecture exhibits a geometrically ordered and periodic framework, representing a highly uniform structure that is absent in conventional foams.

Relative permeability, which characterizes the mobility of each fluid phase within a multiphase porous system, provides additional insights into hydrogen and water transport in the electrodes (Fig. 1g). The highly ordered square electrode

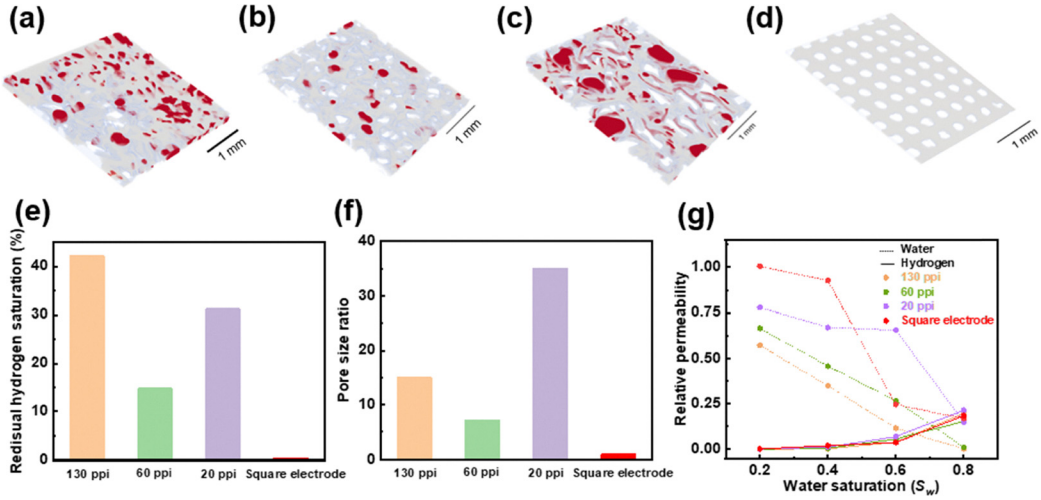

Fig. 1 LBM simulation of liquid and gas transport in the highly ordered square electrode and nickel foams with varying pore densities from segmented micro-CT images. Simulated gas distribution in (a) 60 ppi, (b) 40 ppi, (c) 20 ppi Ni foams, and (d) highly ordered square electrode; grey denotes the electrode substrate, and red represents the gas; (e) residual hydrogen saturation, (f) pore size ratio, and (g) relative permeability.

demonstrates the highest hydrogen permeability, further confirming its superior and highly efficient gas transport behavior. Among the nickel foams, the 20 ppi sample has the highest hydrogen permeability due to its large and open pores, whereas the 130 ppi foam exhibits the lowest because of its smaller pores. The 60 ppi foam has intermediate hydrogen permeability, consistent with its balanced pore size and distribution. These findings highlight the need to balance gas mobility and gas trapping tendency: highly open structures favor gas flow but can increase residual gas retention, while denser porous media enhance solid surface area but suffer from both gas trapping and reduced gas permeability. Therefore, among the foams, the 60 ppi sample represents the optimal compromise, whereas the highly ordered square electrode further achieves the overall best performance.

A highly ordered square-grid electrode was realized through a 3D-printing process (Fig. S2 to S7, SI, with fabrication details in the Methods section). The grid size and beam thickness are fine-tuned to match those of the commercial 60 ppi nickel foam. As the beam thickness was gradually reduced across the printed series, the surface roughness increased (owing to metallization and layer-stepping effects). Microstructure-resolved LBM of the as-prepared 3D-printed highly ordered electrode confirms its well-defined grid morphology and reveals a very low level of residual hydrogen gas saturation. Together, these results demonstrate that the optimally designed highly ordered square-grid electrode possesses geometric parameters comparable to those of conventional foams, *i.e.,* porosity and pore sizes, yet exhibits markedly enhanced gas transport performance. While these findings are invaluable to understand the underlying mechanism, it is equally important to validate them using *operando* characterization methods.

Despite the promises of this technique, conventional lab-based micro-CT is not capable of resolving the dynamic evolution of gas bubbles, as the slow imaging time of the instrument leads to significant differences over the duration of the 3D scan. As a result, pores are either filled with electrolyte (before electrolysis) or fully saturated with gas (after electrolysis) (Fig. S8, SI). Herein, we employed *operando* micro-CT to directly observe gas bubble evolution in porous electrodes under electrochemical operation using an in-house custom-designed compact tubular-shaped *operando* alkaline water electrolyzer (Fig. 2 and Fig. S9, SI; 4 mm inner diameter and 5 mm outer diameter). The properties of the 60 ppi and 130 ppi nickel foams were investigated, as these exhibit markedly different porosities.

We first performed a rapid linear sweep voltammetry (Fig. S10, SI) to evaluate the performance of this compact alkaline water electrolyzer. Both the 60 ppi and 130 ppi nickel foam electrodes exhibited stable polarization behaviour in 1 M KOH containing 30 wt% KI, demonstrating that the cell configuration supports reliable electrolysis performance during simultaneous micro-CT imaging. No visible oxidation peak of I^- appeared, as the oxidation process is masked by anodic oxygen evolution reaction (OER) overpotential at high current densities. Furthermore, minimal heat dissipation was observed using thermal imaging, indicating minimal electrolyte evaporation (Fig. S11, SI). Therefore, all changes in the electrolyte content are attributed to the generation of gas bubbles under constant load.

Previous studies have employed micro-CT imaging to investigate gas–liquid–solid interactions in electrochemical systems, including fuel cells, CO_2 electroreduction, water electrolysis, and batteries.[25–27] In the context of water electrolysis, gas bubble evolution—including gas bubble formation and accumulation, as well as associated evolution in porous electrodes—has been a central topic of micro-CT imaging investigation. However, direct time-resolved three-dimensional observation of dynamic bubble nucleation and growth within thick porous electrodes during active electrolysis remains challenging. Most reported studies *ex situ* capture the gas bubble displacement after a current has been applied for a long period.[25] A more direct approach is *operando* imaging, which captures the dynamics of gas bubble evolution under load in real time.

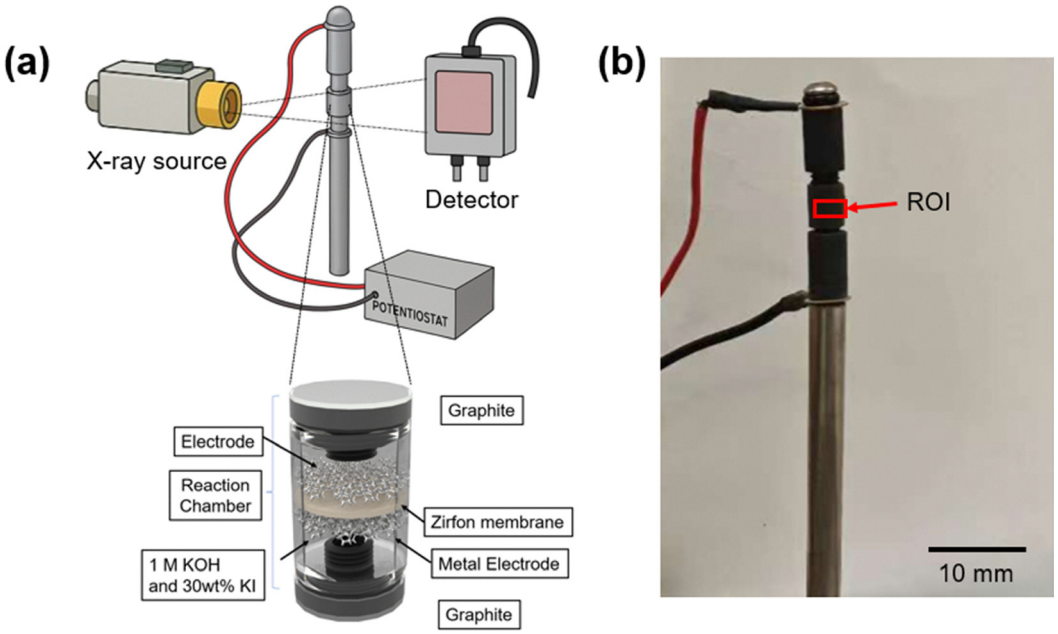

Fig. 2 Design and configuration of the *operando* micro-CT electrolysis cell. (a) Schematic and (b) photograph of the custom *operando* cell for micro-CT imaging of gas evolution.

In this work, bubble generation and growth were captured by continuously measuring *operando* micro-CT 3D tomographs while applying a constant current density of 10 mA cm^{-2} over 300 s at the Australian Synchrotron MCT beamline at room temperature. The *operando* micro-CT measurements in this work do not replicate large-scale industrial alkaline water electrolysis conditions (*e.g.*, ampere-level current density and 80 °C). Instead, they are designed to capture gas bubble dynamics under controlled conditions and to provide insight into the role of electrode geometry.

Each tomograph was acquired in 7 s with an exposure time of 40 ms per projection and a voxel size of 3.6 μm, using a 53.4 keV white beam at the synchrotron. A delay between each 3D tomograph was necessary to return to the original position and reset the instrument. The *operando* micro-CT measurements focused on the HER side, enabling the visualization of hydrogen bubble nucleation and growth dynamics at the cathode during electrolysis. This continuous electrolysis strategy ensured that the electrode remained under steady operating conditions rather than intermittent load cycles, which may disrupt the gas bubble dynamics, allow for electrolyte redistribution, or even cause corrosion. Importantly, within the second-scale window of sequential scans, the reconstructed 3D images showed an incremental change in bubble morphology. These conditions, featuring second-scale acquisition and high resolution, enable real-time bubble imaging that is not achievable with conventional laboratory micro-CT (Fig. S8, SI). Therefore, realizing *operando* micro-CT imaging of bubble evolution requires establishing a well-defined feasibility window through careful balancing of beam conditions, cell geometry, and materials that provide sufficient attenuation contrast between different phases, reaction rate, and electrolyte management. Although 10 mA cm^{-2} current density is lower than the ampere-level current density of industrial systems conditions, the fundamental bubble life cycle and gas–pore interactions remain structurally governed and are only amplified with higher loads.[28] Direct extrapolation to industrial conditions should be made with caution; nevertheless, the results provide novel insight into the influence of electrode structure on bubble dynamics.

Throughout the imaging period, the voltage profile of 60 ppi nickel foam remains steady with minor fluctuations (Fig. 3a). The first six sequential tomograms, accompanied by segmented micro-CT images and aligned with the corresponding timeline, reveal the spatiotemporal evolution of hydrogen gas bubbles within the porous electrode during electrolysis. In the initial stage (Fig. 3a(I), open circuit), the electrode is largely wetted, although some residual air remains trapped within the porous structure. Upon current application (Fig. 3a(II and III)), small, isolated bubbles begin to nucleate along internal ligament surfaces and gradually grow. As the reaction proceeds (Fig. 3a(IV and V)), these hydrogen bubbles coalesce into larger gas pockets while maintaining connectivity with neighboring pore channels. Finally, several large bubbles are observed occupying interconnected voids (Fig. 3a(VI)), demonstrating that the well-connected pore structure facilitates hydrogen bubble transport and removal throughout the electrode during operation. Notably, the relatively open-pore architecture of the 60 ppi foam promotes dynamic bubble behaviour, where enhanced bubble coalescence and displacement are observed—small bubbles continuously merge into larger ones. These features contribute to the minimization of gas trapping and localized mass transport resistance, which in turn is expected to lower concentration overpotentials and improve overall alkaline water electrolyzer efficiency.

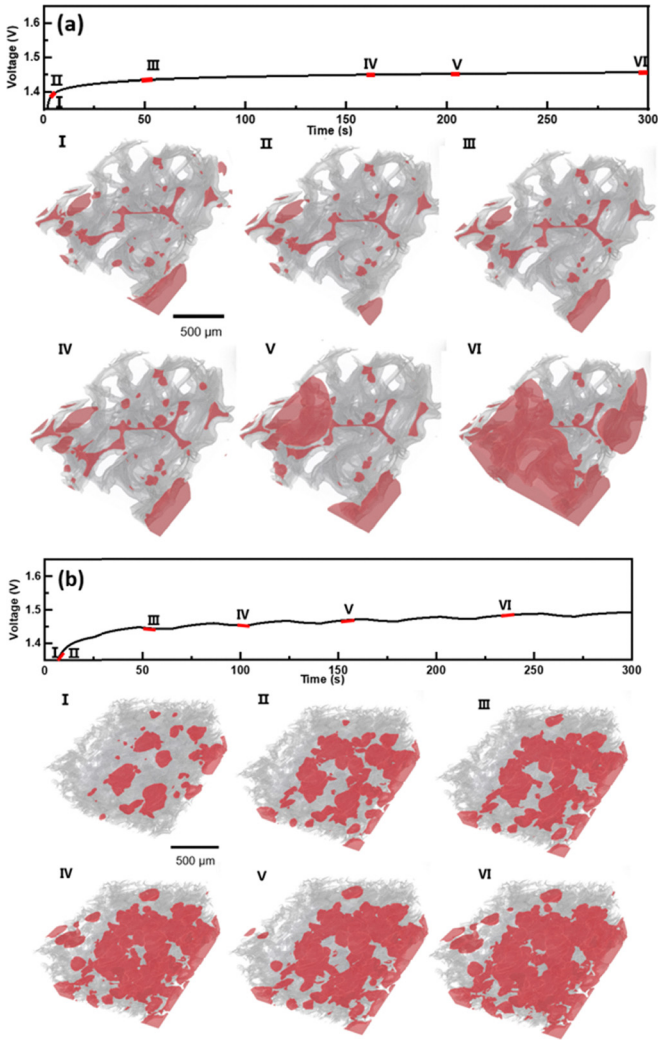

Fig. 3 *Operando* micro-CT visualization of hydrogen gas bubble evolution during alkaline water electrolysis. (a) 60 ppi foam of the voltage–time curve for 300 s under a current density of 10 mA cm^{-2} using 1 M KOH with 30% KI; red markers (I–VI) denote the six tomographic acquisition times used for reconstruction; sequential tomographic cross-sections (panels I–VI) capture the spatiotemporal distribution of gas (red), liquid electrolyte (white), and solid Ni electrode (gray) after 0 s, 4 s, 49 s, 169 s, 204 s and 292 s; (b) 130 ppi foam of voltage–time curve for 300 s under a current density of 10 mA cm^{-2} using 1 M KOH with 30% KI; red markers (I–VI) denote the six tomographic acquisition times used for reconstruction; Sequential tomographic cross-sections (panels b–g) capture the spatiotemporal distribution of gas (red), liquid electrolyte (white), and solid Ni electrode (gray) after 0 s, 7 s, 48 s, 97 s, 207 s and 232 s.

The *operando* micro-CT characterization of 130 ppi foam (Fig. 3b) reveals different hydrogen gas bubble behavior. Throughout the electrolysis period, numerous small hydrogen bubbles persist within the finer pore network and neither migrate nor coalesce. The bubbles thus remain trapped in confined regions, forming localized gas pockets that are slow to detach. This shows that the dense porous structure of the 130 ppi foam restricts gas transport pathways. Moreover, the voltage profile exhibits more frequent and irregular fluctuations in the 130 ppi foam compared to the 60 ppi foam.[29] These voltage oscillations indicate that trapped hydrogen bubbles intermittently block active sites, reflecting inefficient bubble release. The inability to evacuate hydrogen leads to local accumulation, elevated concentration overpotentials, and compromised electrochemical activity. As a result, the 130 ppi foam requires a higher operating voltage to maintain the same current density, further confirming that inefficient gas transport increases the overall overpotential of electrolysis. This interpretation is further supported by the hydrogen saturation analysis based on *operando* micro-CT results, which reveals that the 60 ppi foam structure is more readily occupied with hydrogen gas (Fig. S12, SI). This behaviour reflects more effective gas generation, retention, and transport in the 60 ppi foam, whereas the lower saturation observed in the 130 ppi sample suggests hindered gas accumulation and transport due to limited pore connectivity and higher tortuosity. Therefore, the open pore architecture enhances gas transport and electrolysis performance.

Electrochemical measurements were then performed to elucidate the impact of electrode porosity on overall water electrolysis performance for both the nickel foams, highly ordered square electrodes, and catalyst-coated square electrodes. As shown in H-cell experiments (Fig. S13 and S14, SI), the square electrodes exhibited higher current densities in the high current density regime where bubble generation is more intense, owing to their superior ability to mitigate bubble trapping and promote efficient bubble detachment. Foams with larger pores (20 ppi) exhibited lower intrinsic activity under low voltages, due to reduced surface area. In contrast, the 130 ppi foam displayed higher current densities at low voltages, accompanied by a more pronounced nickel oxidation peak, indicating a greater active nickel surface area, which is also corroborated by LBM simulation (Fig. S15, SI). While the higher surface area endows the 130 ppi foam with superior intrinsic activity, it displays lower current densities at higher potentials. This result suggests that the dense structure of low-porosity nickel foam introduces severe mass transport limitations, hindering reactant diffusion and bubble release. The smaller pore architecture restricts electrolyte access and promotes bubble accumulation, as predicted by LBM simulation and experimentally observed using *operando* micro-CT, thereby slowing interfacial kinetics and compromising electrolysis efficiency under high-rate conditions.

We then compared the electrochemical performances of the nickel foams with different porosities and the highly ordered square electrodes in a membrane electrode assembly (MEA) alkaline water electrolyzer (Fig. 4a and Fig. S16, SI). The highly ordered square electrode outperformed all commercial foams (Fig. 4c), delivering higher current densities at a given voltage than commercial nickel foams (20, 60, and 130 ppi). Its square-like, periodic pore architecture provides straight and uniform transport channels, enables smoother bubble detachment, and markedly reduces voltage fluctuations. The 60 ppi foam consistently outperforms the 20 ppi and 130 ppi ones, which is attributed to a trade-off between sufficient pore volume for effective bubble detachment and adequate structural density to maintain low electronic and ionic resistance within the electrode and across the electrode–membrane interfaces. Importantly, the minimal performance difference observed in

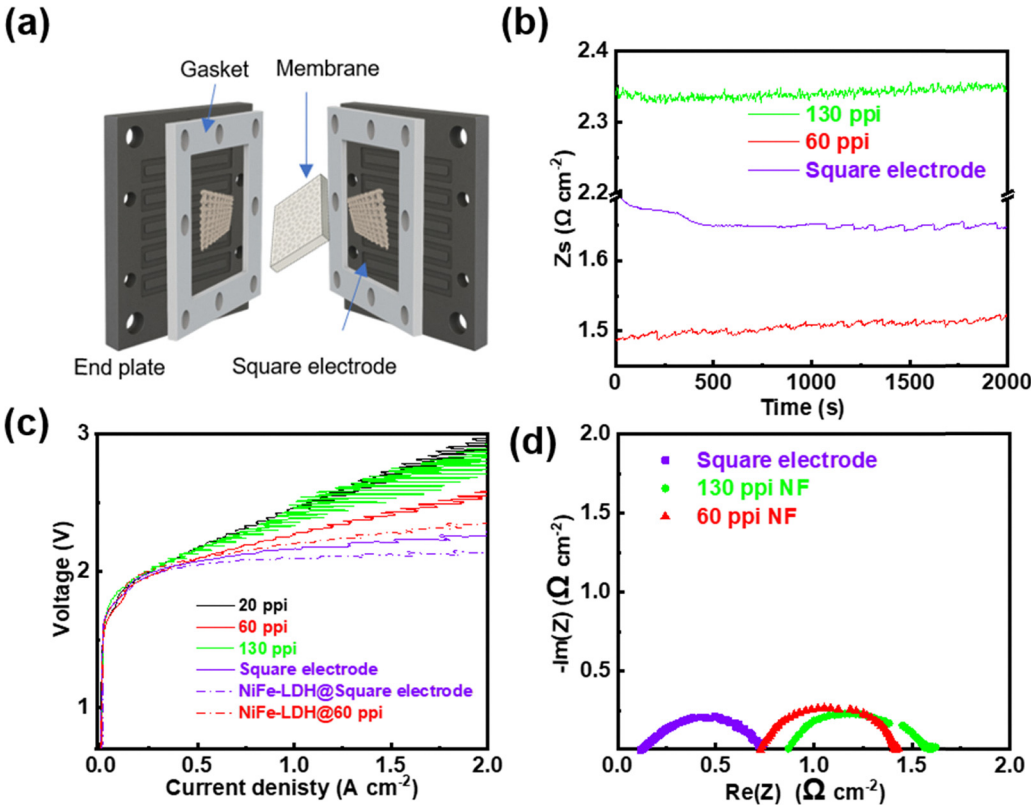

Fig. 4 Comparative electrochemical performance of different electrode architectures. (a) Schematic illustration of the electrolyzer assembly in a square electrode/Zirfon™/square electrode configuration; (b) time-resolved dynamic resistance responses of 60 ppi nickel foam, 130 ppi nickel foam, and highly ordered square electrodes at 20 kHz and 100 mA cm^{-2} current density; and (c) polarization curves showing current density *versus* voltage for alkaline water electrolyzers using nickel foams of different ppi densities and the highly ordered square electrode. Electrolyte: 30 wt% KOH, Zirfon™ UTP 220 membrane, and ambient temperature. (d) Electrochemical impedance spectroscopy measurements of the electrolyzer equipped with a highly ordered square electrode, 60 ppi nickel foam electrode, and 130 ppi nickel foam electrode under a current density of 200 mA cm^{-2}.

H-cell tests at low current densities, particularly at low cell voltages where bubble generation and mass transport limitations are negligible (Fig. S14, SI), indicates comparable intrinsic catalytic activity among the electrodes. The pronounced advantage under high current density MEA conditions, therefore, confirms that the improvement is predominantly structural in origin. The difficulty of bubble removal in denser foams is further evidenced by the severe voltage fluctuations in polarization curves, which are indicative of intermittent blockage and release of gas bubbles during electrolysis.

To decouple the effects of geometric surface area and intrinsic catalytic activity from structural mass transport advantages, we next compare the electrochemically active surface area (ECSA) of the best-performing Ni foam (60 ppi) with that of the square electrode using non-faradaic cyclic voltammetry measurements conducted in the absence of gas bubbles. Although the 60 ppi nickel foam exhibits a significantly larger ECSA (33.9 cm^2) than the highly ordered square electrode (13.8 cm^2) (Fig. S17, SI), the square-grid architecture exhibits markedly faster gas removal and mass transport kinetics as shown in deconvoluted polarization curves. This is consistent with the LBM-predicted lower residual gas saturation and higher effective permeability. As shown in Fig. S18, SI, after ECSA normalization, the highly ordered square electrode consistently delivers higher current densities at a given voltage compared to the 60 ppi Ni foam.

Single-frequency impedance measurements confirm the superior gas bubble dynamics of the highly ordered square electrode, which exhibited the smoothest ohmic resistance profile (Fig. 4b). In contrast, the 130 ppi foam displayed more pronounced fluctuations, reflecting hindered bubble release in its dense, tortuous network, while the 60 ppi foam showed more moderate oscillations. Fourier transform analysis of these fluctuations (Fig. S19, SI) revealed that the square electrode possessed a narrow spectral envelope, indicative of shorter bubble residence times and more efficient detachment dynamics.[28,30] The denser 130 ppi foam exhibited broad low-frequency peaks (<0.05 Hz), characteristic of prolonged bubble accumulation, whereas the 60 ppi foam displayed weaker amplitudes and faster relaxation. This interpretation is corroborated by the smaller mean spectral envelope of the square electrode (Fig. S20, SI), signifying reduced impedance fluctuations and more stable interfacial behavior.

To further elucidate the influence of the pore architecture on mass transfer behavior, full spectra electrochemical impedance measurements were performed under steady-state

electrolysis conditions ranging from 200 to 500 mA cm^{-2} (Fig. 4d and Fig. S21, SI). The highly ordered square electrode exhibits the lowest impedance on the full frequency range among all samples, with a total ohmic resistance of less than 0.2 Ω cm^{-2} at a current density of 200 mA cm^{-2}, compared to 0.75 and 0.85 Ω cm^{-2} for the 60 ppi and 130 ppi foams, respectively. This superior performance arises from its periodic open-lattice architecture, which minimizes bubble coverage under reaction conditions, enhances ion conduction, and facilitates bubble removal. In contrast, the higher resistance observed for the 130 ppi foam can be attributed to restricted reactant diffusion and gas accumulation within its finer pore network, which reduces the effective surface area and compromises electrolysis performance.

When further coated with nickel iron layered double hydroxide catalysts (NiFe-LDH) and Pt on the grid electrode as anode and cathode,[31] the electrolyzer delivered excellent water-splitting performance. At ambient temperature, it required only 2.13 V to reach 2 A cm^{-2} (Fig. 4c). This performance not only surpasses that of the NiFe-LDH-coated 60 ppi foam in this study under identical conditions, but also outperforms that of most literature-reported NiFe-LDH catalysts in alkaline water electrolyzers (Table S2, SI). To further understand the origin of performance differences, the overall polarization was deconvoluted into ohmic, mass transport, and activation contributions (Fig. S22, SI) for both the 60 ppi nickel foam and the highly ordered square-grid electrodes. We find that as the current density increases, the mass transport overpotential of the 60 ppi nickel foam increases significantly, highlighting the severe mass transfer limitations of commercial foams at industrial current densities. In contrast, the highly ordered square-grid structure exhibits a markedly reduced mass transport overpotential compared to that of the 60 ppi nickel foam-based MEA. Quantitatively, the mass transport overpotential at 2 A cm^{-2} for the ordered grid is nearly zero, compared to ~0.25 V for the 60 ppi foam. Notably, at high current densities, the activation overpotential of the ordered electrode is significantly lower than that of the 60 ppi foam. This behavior is likely associated with bubble-induced active-site occlusion in the commercial foam, where accumulated gas coverage reduces the effective operation of the ECSA and consequently increases the apparent activation loss. In contrast, the highly ordered electrode mitigates gas accumulation and concentration polarization, while preserving a larger fraction of the electrochemically accessible surface area under load. As a result, the ordered structure simultaneously suppresses both mass transport and apparent activation losses, enabling more efficient gas–liquid transport and sustained high-rate electrolysis (Notes S2, SI).

Crucially, the superiority of the highly ordered square electrode does not stem from a higher intrinsic activity, but rather from its structural advantages in mass transport, which also makes more active sites accessible and increases the effective activity under high loads. These results reaffirm that structural engineering can be as performance-determining as catalyst selection: even with identical intrinsic activity, minimizing gas trapping directly translates into lower operating voltage and lower charge transfer. Although realized here *via* 3D printing, the geometric design principles demonstrated in this work can translate to more scalable manufacturing routes for industrial alkaline water electrolysis, such as controlling sintering,[32] metal weaving or mesh stacking,[33] or roll-to-roll perforated sheet fabrication.[34]

Our results underscore the critical role of optimized pore size distribution and interconnected porosity in enabling efficient hydrogen evolution, minimizing concentration overpotentials, and sustaining high-rate alkaline water electrolysis. The MEA investigations further highlight that an intermediate and highly ordered architecture provides an effective, rapid bubble detachment, supporting efficient operation under practical cell configurations. Notably, the pronounced differences in performance across foams with varying pore structures and the highly ordered square electrode suggest that bubble accumulation and transport within the porous network are primary factors limiting current output and voltage stability. While electrochemical measurements such as impedance spectra and linear sweep voltammetry (LSV) fluctuations can indirectly reflect bubble behavior, *operando* micro-CT enables direct visualization of these dynamics in real time, while LBM simulations are a critical tool to further examine the mechanism. Synchrotron-based *operando* micro-CT enables direct visualization of dynamic bubble behavior, whereas systematic comparisons across different electrode geometries can be efficiently performed using LBM simulations. By combining real-time imaging, advanced two-phase flow simulations, and performance measurements, we gain a deeper and more mechanistic understanding of how hydrogen gas bubbles evolve and impact the operation of porous electrodes during water electrolysis. Lastly, these results highlight the need to advance dynamic micro-CT imaging toward more industrially relevant operating regimes and a broader range of porous electrode structural designs for various electrochemical systems.

3. Conclusion

In this work, gas bubble dynamics in nickel-based porous electrodes for alkaline water electrolyzers are revealed using synchrotron-based *operando* micro-CT combined with LBM simulations. For the first time, high-resolution hydrogen gas bubble evolution during electrolysis was directly visualized in *operando*, revealing how the pore architecture of the electrode governs bubble behaviour and thus the overall electrochemical performance. The highly ordered square electrode, with its optimized porosity and well-defined geometrical architecture, enables efficient bubble detachment and minimized concentration overpotentials, achieving superior electrochemical performance at 2.13 V and 2 A cm^{-2} in MEA with a 500 μm Zirfon membrane. This highly efficient bubble removal behaviour enhances mass transfer and allows the highly ordered electrode to outperform state-of-the-art benchmark electrodes for alkaline water electrolysis. Our results demonstrate that the geometric surface area alone cannot serve as the sole design criterion for

porous electrodes, as active sites are blocked by gas bubbles trapped within the electrode's porous structure, causing severe mass transport limitations. Looking forward, these findings offer a pathway to scale geometry-engineered electrodes for efficient gas involving reactions.

4. Methods

4.1. Materials

4.1.1. Metal foams. Nickel foams with pore densities of 20, 40, 60, 100, and 130 per unit inch of length (ppi) and a 3 mm thickness were purchased from Kunshan Xingzhenghong Electronic Materials Co., Ltd, China.

4.1.2. Highly ordered electrodes fabricated by 3D printing. The highly ordered square electrodes were fabricated using direct metal laser sintering on an EOSINT M 280 system (3DNewshape, France). The material used was Inconel 625 powder (58% Ni, 20–23% chromium), with a particle size distribution of 15–45 μm. The powder morphology was spherical, ensuring optimal flowability and packing density during recoating. A laser power of 290 W, a scan speed of 1200 mm s^{-1}, a hatch spacing of 0.10 mm, and a layer thickness of 50 μm were used to achieve the desired features. Stripe scanning with layer-by-layer rotation was used to minimize residual stress and thermal buildup. The chamber was maintained under high-purity nitrogen (<0.2% O_2), and the baseplate was preheated to 80 °C to reduce thermal gradients. Post-processing included powder removal *via* air blasting and ultrasonic cleaning. The resulting 3D-printed inconel blocks have external dimensions of 40 mm × 40 mm × 40 mm. Each 3D-printed inconel block featured a 0.2 mm strut diameter, with unit cell spacing varying between 0.3 mm and 0.8 mm. The blocks were subsequently machined into thin slices (500 μm) for electrochemical testing in alkaline water electrolyzers, and into cylindrical pellets (3 mm in diameter and 2 mm in height) for *operando* cell measurements.

4.1.3. Catalyst electrodeposition. The electrochemical coating of NiFe-layered double hydroxide (NiFe-LDH) on the square electrode as the anode was carried out following previously reported methods.[31] Specifically, a 1 × 1 cm^2 electrode was immersed in an aqueous electrolyte containing equal molar (3 mM) concentrations of $Ni(NO_3)_2{\cdot}6H_2O$ and $Fe(NO_3)_3{\cdot}9H_2O$. The electrodeposition was conducted in a standard three-electrode cell with the square electrode as the working electrode, a graphite plate as the counter electrode, and an Ag/AgCl (3 M KCl) electrode as the reference. A constant potential of −1.0 V (*vs.* Ag/AgCl) was applied for 300 s at 10 °C, during which nitrate ions were reduced to generate local hydroxide ions, enabling the co-deposition of Ni^{2+} and Fe^{3+} into bimetallic hydroxide deposits on the electrode surface. The cathode was a platinum-coated substrate, obtained by depositing a thin Pt layer on the square electrode *via* sputter coating for 30 s. The same electrodeposition parameters were applied to all substrate types, including the commercial nickel foam electrodes and the 3D-printed electrode. This ensured consistent catalyst loading conditions and enabled a direct comparison of structural effects independent of variations in surface chemistry. Therefore, catalyst loading procedures and operating conditions were controlled to ensure comparability across different electrodes.

4.2. Characterization studies

4.2.1. X-ray micro-CT experiments. X-ray micro-CT imaging was performed at the MCT beamline of the Australian Synchrotron. A white beam with an energy of 45.466 keV was used in combination with a CMOS-based white beam detector. Multiple filters were applied, including diamond (70.9 mm position, 0.2 mm thickness), aluminum (11 mm position, 5 mm thickness), copper (39 mm position, 0.5 mm thickness), and palladium (43.5 mm position, 0.05 mm thickness), to optimize beam quality. Tomographic scans were acquired with a rotation step of 0.10032°, yielding 1820 projections with an exposure time of 0.04 s per projection. In each cycle, the micro-CT system acquired a complete 3D scan over 7 seconds, followed by a 37-second instrument reset. The field of view was 9.25 mm (length) × 4 mm (width), with image dimensions of 2560 × 2560 × 760 voxels, corresponding to a pixel size of 3.6 μm. This setup enabled high-resolution three-dimensional reconstruction of gas–liquid distributions within the porous electrodes during electrochemical operation. Laboratory micro-CT measurements were also performed on a TESCAN CoreTOM system (120 kV, 80 μA), requiring ∼16 s per scan (74 s reset) with a voxel size of 21 μm. For image segmentation, the reconstructed datasets were denoised using a non-local means filtering algorithm, followed by multi-Otsu thresholding to separate the different materials. All image processing was conducted using the scikit-image library in Python.[35] The eight reconstructed 3D images were further converted into a time-lapse video using ParaView to visualize the dynamic gas–liquid evolution within the porous electrode. Phase segmentation and quantitative porosity calculations were performed using Avizo based on grayscale thresholding of the segmented phases.[36]

4.2.2. Scanning electron microscopy. Micrographs of the nickel foams with different porosities and 3D-printed electrodes with various cell spacings were captured using a scanning electron microscope. Images showing the surface morphology and pore structures were obtained using a Hitachi TM4000Plus Benchtop SEM, which is equipped with a variable pressure mode allowing imaging of conductive and non-conductive samples without extensive sample preparation.

4.2.2. Optical microscopy. Optical micrographs of nickel foams with different porosities and 3D-printed electrodes with various cell spacings were captured using a stereo zoom microscope (Zeiss, Axio Zoom V16) to characterize their surface morphology and pore structures. The images were used to examine the surface topography and structural differences among the electrodes.

4.2.3. Electrochemical characterization. All electrochemical measurements were carried out using a CHI760E potentiostat with a booster. Electrochemical characterization studies were conducted to evaluate the performance of nickel foams with varying porosities (20 to 130 ppi) under different operating conditions (H-cells and a self-assembled alkaline water electrolyzer). Chronopotentiometry

and linear sweep voltammetry were performed in the custom-designed *operando* electrolyzer described above. Linear sweep voltammetry was conducted from 0 to 3 V at a scan rate of 0.1 V s^{-1} to assess overall cell resistance and performance. Linear sweep voltammetry was conducted at a scan rate of 10 mV s^{-1} without IR compensation. For *operando* micro-CT experiments, the cell first reached equilibrium under open circuit conditions for 300 seconds. This was followed by 300 s at 10 mA cm^{-2}, during which *operando* micro-CT imaging was performed around every 50 seconds. In this work, the current density during the reaction is defined using the planar membrane–electrode contact area (A cm^{-2}). In addition, the current density can be normalized to a volumetric current density (A cm^{-3}) for the membrane electrode assembly, adopting an electrode thickness of 500 μm.

Electrochemical impedance spectroscopy measurements were performed on the assembled electrolyzer under steady-state operation at current densities from 200 to 500 mA cm^{-2}. The frequency range spanned from 1000 kHz to 10 mHz with an AC amplitude of 0.2 V, allowing for the evaluation of charge-transfer resistance and mass transport characteristics.[37] To observe gas bubble dynamics during the reaction, single-frequency impedance measurement was conducted at 20 kHz under different HER and OER potentials, as well as whole water splitting at different voltages with an amplitude of 0.01 V and a sampling rate of 2 s.[30] The fast Fourier transform (FFT) of the current spectra revealed characteristic frequency features, where higher frequency amplitudes corresponded to faster gas bubble evolution. The extracted FFT patterns of the dynamic resistance variations further illustrate how the detected gas bubble evolution is manifested during reaction (Notes S1, SI). The electrochemical surface areas (ECSAs) of the catalysts were estimated from the double-layer capacitance (C_{dl}), measured by cyclic voltammetry at various scan rates in the nonfaradaic region.[38]

$$j = \nu C_{dl} \quad (1)$$

$$\mathrm{ECSA} = C_{dl}/C_s \quad (2)$$

where j, ν, and C_s are the double-layer charging current densities, scan rates, and specific capacitance (25 μF cm^{-2}), respectively.

4.2.4. Electrochemical cells

4.2.4.1. H-cells. A two-compartment H-cell separated by a Zirfon™ UTP 220 membrane with a thickness of 500 μm was first employed to evaluate the intrinsic electrocatalytic activity. Nickel foams with various porosities (20 to 130 ppi) and highly ordered square electrode with catalysts were tested as anodes and cathodes in 30 wt% KOH at ambient temperature. LSV was performed from 0 to 3 V at a scan rate of 10 mV s^{-1}.

4.2.4.2. Self-assembled alkaline water electrolyzer. A full alkaline water electrolyzer (electrode/Zirfon/electrode) was assembled using membrane–electrode assemblies (MEA) with a surface area of 1 cm^2. Square electrode and Ni foams with different porosities were employed as both the anode and the cathode, and a Zirfon™ UTP 220 membrane was used as the separator.[39] All the Ni foams were compressed under a pressure of 20 kPa into thin sheets with a thickness of 500 μm. The MEA was sandwiched between 75 μm-thick PTFE gaskets to ensure uniform compression and reliable sealing. Stainless steel end plates with embedded current collectors provided robust electrical contact and mechanical stability. The device was operated at ambient temperature with 30 wt% KOH as the electrolyte. The electrolyte was circulated on both the cathode and anode sides using two peristaltic pumps (SHENCHEN, LabS3) at flow rates of 38 mL min^{-1} and 19 mL min^{-1}, respectively, to account for the stoichiometric difference in the hydrogen and oxygen evolution rates. The capillary number in an alkaline water electrolyzer at 1 A cm^{-2} is on the order of 10^{-5}, with capillary $H_2 \approx 5.6 \times 10^{-5}$ at the cathode and capillary $O_2 \approx 2.8 \times 10^{-5}$ at the anode, which display capillary-dominated properties. The capillary number (Ca) is calculated using the following equation:[22]

$$\mathrm{Ca} = \frac{\mu U}{\gamma \cos\theta}, \quad U = \frac{j}{nF}\frac{RT}{P} \quad (3)$$

where μ is the electrolyte viscosity, U is the characteristic gas velocity, γ is the gas–liquid surface tension, θ is the contact angle, j is the current density, n is the number of electrons, F is the Faraday constant, R is the gas constant, T is the temperature, and P is the pressure, under ideal conditions (30 wt% KOH, 298 K, 1 A cm^{-2}, $\theta = 45^\circ$, 1 atm).

For the deconvolution of LSV curves in the MEA, the overall cell voltage (E_{cell}) can be expressed as the sum of the reversible cell potential (E_0) and three main overpotentials: activation ($\eta_{activation}$), ohmic (η_{ohmic}), and mass transport ($\eta_{transport}$), following a typical and widely adopted methodology reported for water electrolysis systems.[39] The η_{ohmic} term was derived from the open circuit impedance compensation results, according to:

$$\eta_{ohmic} = j \times \mathrm{HFR} \quad (4)$$

where j is the current density (A cm^{-2}) and HFR is the resistance (Ω cm^2).

The raw polarization curves were corrected for ohmic losses to obtain the $E_{ohmic\text{-}corrected}$ potentials. From these corrected curves, Tafel slopes were determined in the low-current-density region and extrapolated to higher current densities to estimate $E_{activation}$.

The reaction activation overpotential was characterized using a Tafel slope (b) of LSV:

$$\eta_{activation} = b \times \log\left(\frac{j}{j_0}\right) \quad (5)$$

The transport overpotential ($\eta_{transport}$) was then calculated using:

$$\eta_{transport} = E_{ohmic\text{-}corrected} - E_{activation} \quad (6)$$

4.2.4.3. Operando micro-CT alkaline water electrolyzer. To enable real-time visualization of hydrogen gas bubble evolution during electrochemical water electrolysis, a custom-designed alkaline water electrolyzer cell was developed for synchrotron micro-CT imaging. The cell was engineered to support *operando*

gas evolving electrolysis and X-ray transparency, while remaining electrochemically compatible with a standard potentiostat system (CHI 760E) through direct connection for controlled electrochemical operation. The cell body was constructed from X-ray-transparent polyether ether ketone (PEEK) and featured an aligned cylindrical reaction chamber of 4 mm inner diameter and 5 mm outer diameter. A 4 mm diameter Zirfon™ UTP 220 membrane, which physically separates the anodic and cathodic compartments while permitting ion transport, was sandwiched between two circular 3 mm diameter Ni foam electrodes. Graphite rods were used as current collectors, offering excellent electrical conductivity and chemical stability in high-corrosion environments. To enhance X-ray contrast between hydrogen gas and electrolyte, 30 wt% KI was added to the electrolyte (1 M KOH) as a contrast agent. This high-iodide formulation increased X-ray attenuation in the liquid, facilitating bubble identification and segmentation during tomographic reconstruction. Electrical connections were established by attaching the working electrode to the negative terminal and the counter electrode to the positive terminal of the potentiostat (CHI 760E). A constant current density of 10 mA cm^{-2} was continuously applied throughout the entire measurement process over 300 s while performing manually controlled X-ray tomography (7 s imaging, 37 s return to initial position). The imaging conditions were selected to resolve bubble nucleation and transport dynamics under controlled electrochemical operation. Thermal imaging was performed at a current density of 10 mA cm^{-2} for 30 seconds using a FLUKE VT06 infrared camera to monitor the heat release.

4.3. Lattice Boltzmann method

To model the dynamics of immiscible two-phase flow in porous structures, we use a color-gradient-based lattice Boltzmann framework.[40] The method integrates a multi-relaxation time (MRT) scheme for enhanced numerical stability. We adopt a dual-lattice approach: the D3Q19 lattice handles momentum transport, while the D3Q7 lattice is used for evolving the mass distribution of the individual fluid components. This choice reflects an optimization: since the stress tensor does not appear in the scalar mass transport equation, the computationally lighter D3Q7 scheme provides sufficient resolution without undermining physical fidelity.[41] The evolution of the distribution functions A_q and B_q for the respective fluid components is governed by:

$$A_q\left(x+\xi_q\delta t, t+\delta t\right) = w_q N_a\left[1+\frac{u\cdot\xi_q}{{c_s}^2}+\beta\frac{N_b}{N_a+N_b}n\cdot\xi_q\right] \quad (7)$$

$$B_q\left(x+\xi_q\delta t, t+\delta t\right) = w_q N_b\left[1+\frac{u\cdot\xi_q}{{c_s}^2}-\beta\frac{N_a}{N_a+N_b}n\cdot\xi_q\right] \quad (8)$$

here, N_a and N_b are the mass densities of each component, and ξ_q, w_q, and u represent the discrete lattice velocity, directional weight, and fluid velocity, respectively. The term β controls the sharpness of the interface, while n is the local normal to the interface, derived from the color gradient.

The momentum field evolves through the distribution function f_q:

$$f_q(x_i+\xi_q\Delta t, t+\Delta t) = f_q(x_i, t) + J(x_i, t) \quad (9)$$

with the collision term J incorporating both relaxation processes and external body forces. In all simulations, fluid flow was modeled under capillary-dominated conditions (Ca $\approx 10^{-5}$), with the wettability of the porous medium set to a water-wet regime. This assumption is representative of the hydrogen evolution reaction in alkaline media, whereby hydrophobicity is critical to detach gas bubbles for both precious metal-based and precious metal-free electrodes.[22–24] While wettability can influence the absolute level of gas retention, the relative transport trends identified in this work are primarily governed by pore architecture. All the flow simulations were conducted under comparable flow regimes, boundary conditions, and domain sizes.

The density and viscosity ratios between liquid and gas phases were set to 830 and 245, respectively. In lattice units, gas density = 1 and relaxation time = 2. Interfacial tension was imposed *via* the color gradient formulation and calibrated to a physical surface tension of 60 mN m^{-1}. To evaluate gas trapping potential across different porous media, a constant flux boundary condition was employed at the inlet normal to the flow direction to enforce a fixed injection rate. The porous domain was initially saturated with gas, after which water was injected to displace the non-wetting gas until residual gas saturation was achieved.

To assess the relative permeability of fluids (defined as the ratio of effective to absolute permeability), periodic boundary conditions were utilized to simulate the co-injection of both phases and to minimize boundary effects. In this setup, both fluids were initially distributed randomly within the domain. The lattice Boltzmann method (LBM) was then employed to evolve the fluid–fluid interfaces until a steady-state condition was reached.

The effective permeability (k) for each fluid is determined using the multiphase extension of Darcy's law:

$$k_i = \frac{u_i\mu_i}{\nabla p_i} \quad (10)$$

where u_i is the fluid's velocity in the direction of flow, μ_i is its dynamic viscosity, and ∇p_i denotes pressure gradient. The subscript i refers to either the wetting phase or the non-wetting phase.

The average flow velocity of each fluid phase is calculated from the ratio of its total momentum P_i to its total mass M_i, as given by:

$$\langle u\rangle_i = \frac{P_i}{M_i} \quad (11)$$

Author contributions

S. W., Q. M., P. M., Y. D. W., and C. Z.: conceived and designed the experiments. S. W., O. T., Q. M., Y. D. W., and P. M.: methodology. S. W., O. T., Q. M., Y. D. W., R. A., C. Z., P. M.,

M. R., D. A.-P., H. G., and C. S. investigation. Q. M., R. A., C. Z., P. M., and Y. D. W.: funding acquisition. Q. M., R. A., C. Z., P. M., Y. D. W.: supervision. S. W., O. T., and Q. M.: writing the paper. M. R., C. S., D. A.-P., H. G., Y. D. W., R. A., C. Z., and P. M.: writing – review & editing.

Conflicts of interest

The authors declare no competing interests.

Data availability

The data supporting the findings of this study are available within the article and its supplementary information (SI). Supplementary information is available. See DOI: https://doi.org/10.1039/d6ee00290k.

Acknowledgements

This work was supported by TotalEnergies. The authors acknowledge 3DNewshape and Stéphane Martinez for 3D printing support and the Australian Synchrotron for providing access to the micro-CT beamline. The authors also thank Dr Andrew Stevenson, Dr Benedicta Arhatari, and Dr Ruwini Ekanayake at the Australian Synchrotron for their technical support. The authors also thank Dr Daniel Morris and Dr Amalia Halim at the UNSW Mark Wainwright Analytical Centre for access to advanced characterization facilities and for their assistance with X-ray micro-CT scanning. Chuan Zhao acknowledges support from the Australian Research Council (CE230100017, DP250101509, IC200100023, and FL250100099). Quentin Meyer acknowledges support from the Australian Economic Accelerator (AE240300136). The authors also thank Yang Xiao, Zhun Shi, Muhammad Akbar, Haochen Lu, Dr Wen Xi, and Umar Alfazazi at UNSW for their assistance in organizing and preparing the experiments and figures.

References

1 R. Iwata, L. Zhang, K. L. Wilke, S. Gong, M. He, B. M. Gallant and E. N. Wang, *Joule*, 2021, **5**, 887–900.
2 K. Dastafkan, S. Wang, C. Rong, Q. Meyer, Y. Li, Q. Zhang and C. Zhao, *Adv. Funct. Mater.*, 2022, **32**, 2107342.
3 P. A. Kempler, R. H. Coridan and L. Luo, *Chem. Rev.*, 2024, **124**, 10964–11007.
4 H. Ikeda, R. Misumi, Y. Kojima, A. A. Haleem, Y. Kuroda and S. Mitsushima, *Int. J. Hydrogen Energy*, 2022, **47**, 11116–11127.
5 Y. He, Y. Cui, Z. Zhao, Y. Chen, W. Shang and P. Tan, *Energy Rev.*, 2023, **2**, 100015.
6 A. Taqieddin, R. Nazari, L. Rajic and A. Alshawabkeh, *J. Electrochem. Soc.*, 2017, **164**, E448.
7 J. Park, M. J. Kim, Y. Kim, S. Lee, S. Park and W. Yang, *ACS Energy Lett.*, 2024, **10**, 212–237.
8 Y. Li, Z. Y. Fu and B. L. Su, *Adv. Funct. Mater.*, 2012, **22**, 4634–4667.
9 O. A. Ibrahim, M. Navarro-Segarra, P. Sadeghi, N. Sabaté, J. P. Esquivel and E. Kjeang, *Chem. Rev.*, 2022, **122**, 7236–7266.
10 Y. Luo, L. Wang, J. Sun, Q. Chen, Z. Wang, M. Zheng and Y. Hou, *Int. J. Hydrogen Energy*, 2025, **142**, 168–179.
11 F. Liu, F. Wang, X. Hao, Z. Fan and J. Tan, *Chem. Eng. Sci.*, 2024, **298**, 120307.
12 N. K. Chaudhari, H. Jin, B. Kim and K. Lee, *Nanoscale*, 2017, **9**, 12231–12247.
13 F. Rocha, R. Delmelle, C. Georgiadis and J. Proost, *J. Environ. Chem. Eng.*, 2022, **10**, 107648.
14 J. T. Lang, D. Kulkarni, C. W. Foster, Y. Huang, M. A. Sepe, S. Shimpalee, D. Y. Parkinson and I. V. Zenyuk, *Chem. Rev.*, 2023, **123**, 9880–9914.
15 M. J. Blunt, B. Bijeljic, H. Dong, O. Gharbi, S. Iglauer, P. Mostaghimi, A. Paluszny and C. Pentland, *Adv. Water Resour.*, 2013, **51**, 197–216.
16 E. Leonard, A. D. Shum, S. Normile, D. C. Sabarirajan, D. G. Yared, X. Xiao and I. V. Zenyuk, *Electrochim. Acta*, 2018, **276**, 424–433.
17 I. V. Zenyuk, *Curr. Opin. Electrochem.*, 2019, **13**, 78–85.
18 O. Panchenko, E. Borgardt, W. Zwaygardt, F. J. Hackemüller, M. Bram, N. Kardjilov, T. Arlt, I. Manke, M. Müller and D. Stolten, *J. Power Sources*, 2018, **390**, 108–115.
19 C. Dunlap, C. Li, H. Pandey, N. Le and H. Hu, *J. Appl. Phys.*, 2024, **136**, 014902.
20 S. Ferdoush, S. B. Kzam, P. H. Martins, J. Dewanckele and M. Gonzalez, *Int. J. Pharm.*, 2023, **648**, 123565.
21 P. Mostaghimi, M. Liu and C. H. Arns, *Math. Geosci.*, 2016, **48**, 963–983.
22 C. Lee, J. Hinebaugh, R. Banerjee, S. Chevalier, R. Abouatallah, R. Wang and A. Bazylak, *Int. J. Hydrogen Energy*, 2017, **42**, 2724–2735.
23 K. Peng, W. Guo, G. Wang, P. Cui, Z. Chen, Z. Guo, X. Zhang, Y. Zeng and J. Jiang, *Nano Res.*, 2026, **19**, 94908046.
24 W. Du, L. Fan, J. Han, B. Wang, X. Li, C. Tongsh, Z. Wang and S. Liu, *J. Power Sources*, 2026, **662**, 238771.
25 K. Köble, A. Ershov, K. Duan, M. Schilling, A. Rampf, A. Cecilia, T. Faragó, M. Zuber, T. Baumbach and R. Zeis, *J. Energy Chem.*, 2024, **91**, 132–144.
26 Y. Chen, G. Stelmacovich, A. Mularczyk, D. Parkinson, S. K. Babu, A. Forner-Cuenca, S. Pylypenko and I. V. Zenyuk, *ACS Catal.*, 2023, **13**, 10010–10025.
27 S. J. Altus, B. J. Inkson and J. Hack, *J. Mater. Chem. A*, 2024, **12**, 23364–23391.
28 X. Zhao, H. Ren and L. Luo, *Langmuir*, 2019, **35**, 5392–5408.
29 M. He, K. Fic, E. Fra, P. Novák and E. J. Berg, *Energy Environ. Sci.*, 2016, **9**, 623–633.
30 K. Dastafkan, S. Wang, S. Song, Q. Meyer, Q. Zhang, Y. Shen and C. Zhao, *EES Catal.*, 2023, **1**, 998–1008.
31 X. Lu and C. Zhao, *Nat. Commun.*, 2015, **6**, 1–7.
32 T. Rauscher, C. I. Bernäcker, S. Loos, M. Vogt, B. Kieback and L. Röntzsch, *Electrochim. Acta*, 2019, **317**, 128–138.
33 H. I. Lee, H.-S. Cho, M. Kim, J. H. Lee, C. Lee, S. Lee, S.-K. Kim, C.-H. Kim, K. B. Yi and W.-C. Cho, *Front. Chem.*, 2021, **9**, 787787.

34 R. L. G. Barros, J. Scholl, I. Hoedemakers, X. L. Liang, K. Skadell, J. van der Schaaf and M. T. de Groot, *J. Power Sources*, 2025, **630**, 236116.
35 S. Van der Walt, J. L. Schönberger, J. Nunez-Iglesias, F. Boulogne, J. D. Warner, N. Yager, E. Gouillart and T. Yu, *PeerJ*, 2014, **2**, e453.
36 N. Otsu, *Automatica*, 1975, **11**, 23–27.
37 Q. Meyer, S. Liu, K. Ching, Y. Da Wang and C. Zhao, *J. Power Sources*, 2023, **557**, 232539.
38 C. C. McCrory, S. Jung, J. C. Peters and T. F. Jaramillo, *J. Am. Chem. Soc.*, 2013, **135**, 16977–16987.
39 I. O. Baibars, H. Huang, Y. Xiao, S. Wang, Y. Nie, C. Jia, K. Dastafkan and C. Zhao, *Energy Environ. Sci.*, 2025, **18**, 6248–6259.
40 J. E. McClure, Z. Li, M. Berrill and T. Ramstad, *Comput. Geosci.*, 2021, **25**, 871–895.
41 J. E. McClure, J. F. Prins and C. T. Miller, *Comput. Phys. Commun.*, 2014, **185**, 1865–1874.